



Wainwright, T. R. O., Poole, D. J., Allen, C. B., & Appa, J. (2021). High-Fidelity Aero-Structural Simulation of Occluded Wind Turbine Blades. In *2021 AIAA SciTech Forum* American Institute of Aeronautics and Astronautics Inc. (AIAA).
<https://doi.org/10.2514/6.2021-0950>

Peer reviewed version

Link to published version (if available):
[10.2514/6.2021-0950](https://doi.org/10.2514/6.2021-0950)

[Link to publication record in Explore Bristol Research](#)
PDF-document

This is the author accepted manuscript (AAM). The final published version (version of record) is available online via AIAA at <https://doi.org/10.2514/6.2021-0950>. Please refer to any applicable terms of use of the publisher.

University of Bristol - Explore Bristol Research

General rights

This document is made available in accordance with publisher policies. Please cite only the published version using the reference above. Full terms of use are available:
<http://www.bristol.ac.uk/red/research-policy/pure/user-guides/ebr-terms/>

High-Fidelity Aero-Structural Simulation of Occluded Wind Turbine Blades

Thomas R. O. Wainwright*, Daniel J. Poole†, Christian B. Allen‡
Department of Aerospace Engineering, University of Bristol, Bristol, UK, BS8 1TR

Jamil Appa§, Oliver Darbyshire¶
Zenotech Ltd, Bristol, BS16 1EJ, UK

A coupled, high-fidelity simulation framework on GPUs is presented, and is used to perform an aero-structural simulation of large wind turbines, where a turbine is fully-occluded in the wake of another. The GPU-enabled flow solver, zCFD, is coupled with a modal structural model using a multi-variate volume interpolation with radial basis functions (RBFs). Forces and displacements are transferred between non-coincident aerodynamic and structural models through the interpolation. A multi-scale RBF mesh deformation scheme is then used to propagate displacements through the volume mesh. A fully-meshed turbine in freestream flow is modelled, as well as two turbines at five diameters separation. The turbine blades are modified IEA 15MW blades run at the maximum IEA 15MW loading condition (95ms^{-1} tip speed in flow at 25ms^{-1}). A 10 million cell aerodynamic mesh is used to ensure sufficient capture and transport of the upstream turbine wake. Converged simulations of a fully occluded turbine are presented, as well as aerodynamic simulations of isolated and occluded turbines.

I. Introduction

Climate change, driven primarily by man-made increases in greenhouse gas concentrations, is one of the most important factors in governmental policy making globally. This is set against the backdrop of global population increase (which is set to reach 9.7 billion in 2050 [1]), and the continual increase in global living standards causing an exponential increase in the desire for energy [2]. As such, a substantial drive in the development of low-emission energy production methods has been occurring such that now, low-emission sources account for a substantial fraction of energy production globally.

Harvesting energy from the wind has evolved to become one of the prime alternative fuel sources. Wind turbines harvest energy by converting kinetic energy present in the atmosphere, to rotational kinetic energy, and then to electricity through the use of a generator. The efficiency of the first phase of this process is dictated by the aerodynamic efficiency of the turbine blade. It is therefore critical to ensure these blades operate as close to their theoretical maximum as possible [3].

Advances in composite design and manufacturing technology has allowed for increasingly large rotor diameters, maximising the energy extracted by any one turbine. This trend is seen in the increasing rotor diameters in both reference wind turbines such as the IEA 5MW and DTU 10MW turbines [4, 5], as well as commercial turbines such as the GE Haliade X and Siemens SG 14-222 [6, 7] However, these longer, more flexible blades are prone to strong interaction between aerodynamic and structural dynamics during both operation and down-time. This interaction is often termed Fluid Structure Interaction or FSI. While rotational forces can act to dampen such interactions, non-uniformities in, for example, oncoming flow characteristics found during operation can excite interactions.

The preferred method of deployment for wind turbines is in large-scale compact farms, minimising the geological footprint of the farm, and reducing the required infrastructure for a fixed number of turbines. The issue arising from farm layouts is that for any given wind direction, due to turbines yawing to the local wind direction in an attempt to maximise a turbine's individual power production, it is highly likely one or more turbines will be fully or partially occluded by the wake of an upstream turbine. A simple example showing different occlusion levels of a downstream

*PhD Candidate, Email: tom.wainwright@bristol.ac.uk

†Lecturer in Aerodynamics, AIAA Member, Email: d.j.poole@bristol.ac.uk

‡Professor of Computational Aerodynamics, AIAA Senior Member, Email: c.b.allen@bristol.ac.uk

§Co-Founder and Director at Zenotech Ltd, Email: jamil.appa@zenotech.com

¶Lead CFD Engineer, Email: oliver.darbyshire@zenotech.com

turbine due to the wake of an upstream turbine is shown in Figure 1. This can have severe implications both on the power extracted by the downstream turbine due to momentum deficit in the wake, and the fatigue life of the downstream turbine blades due to buffeting from vortices shed from the upstream turbine. With the wind energy sector tending towards turbines using longer, more flexible blades, the ability to accurately simulate high fidelity FSI between the blades and air in a wide range of operational conditions is of increasing interest.

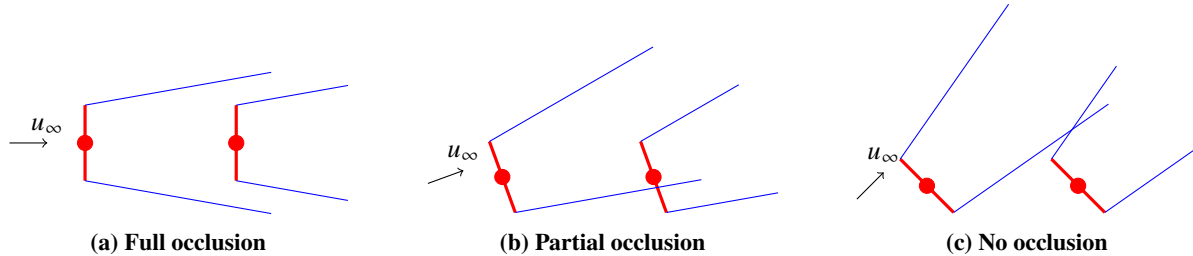


Fig. 1 Example of fully-occluded, partially-occluded and un-occluded downstream turbine (turbines in red, wake boundaries in blue)

Increasing amounts of attention have been paid to the FSI simulation and optimisation of individual turbines under free stream conditions; see [8, 9] for example. However, the importance of determining fatigue and operational stability of inner-farm turbines is ever increasing, particularly as more field data is obtained about the long term fatigue behaviour of first generation wind turbines where full or partial occlusion is apparent. Oncoming flow characteristics due to occlusion are complex, and often time-dependent due to the nature of wakes shed from upstream turbines. As such, high-fidelity simulation is necessary to understand the impact of occlusion on efficiency, loads and fatigue, however little work has been attempted in this area, particularly on FSI.

The aim of this paper is to demonstrate a high fidelity FSI coupling scheme for simulation of wind turbines. In this paper, steady state FSI modelling of turbine occlusion is considered to determine deeper insight into this aspect of operation. Development of a large-scale multi-physics solver is presented that is based on computational fluids dynamics (CFD) solver, zCFD* and an advanced structural model developed in house at the University of Bristol, coupled together with a generic volume interpolation-mesh motion strategy based on radial basis functions and without the need for point reduction. Furthermore, graphics processing units (GPUs) are exploited to vastly improve run-times and make run-times of such high-fidelity coupled simulations possible within a few hours.

II. Background

A review of relevant FSI simulation methods relevant to this work is presented here. For a more in-depth review of numerical methods specifically applied to wind turbine simulations, the reader is directed to the review papers by O'Brien *et al.* [10], Bai and Wang [11], and Thé and Yu [12].

Historically the high cost associated with full CFD simulation of a wind turbine has led to the development of lower fidelity methods, which provide a satisfactory aerodynamic result at a much lower cost. For near wake aerodynamic studies the actuator line and surface models developed at DTU [13–15] have been used in conjunction with LES to provide a good flow structure. These methods provide a framework for generating the aerodynamic effects of the moving blades to the flow, without having to obtain a full CFD solution. In most cases the aerodynamic effects of the blades are calculated using Blade-Element-Momentum Theory (BEM).

BEM applies two-dimensional aerodynamic coefficients to a series of finite points along the blade [3]. These coefficients are calculated through the interpolation of lookup tables, generated using two-dimensional potential methods such as XFOIL. Through circumventing the need to perform a full CFD solution of the blade, BEM methods are computationally much cheaper, so have found favour for studies where a high number of calculations must be performed but aerodynamic accuracy is not the prime focus, such as structural optimisation [16–18]. Low fidelity alternatives to BEM is have also been explored, such as the panel method developed by Boujleben *et al* [19], and a lifting line method, as implemented by Sessarego *et al* [20].

The major issues with BEM are that it does not account for span-wise flow effects, and it performs poorly around stall conditions. This makes it inappropriate for application for high Tip-Speed Ratio (TSR) turbines, and turbines

*<https://zcfid.zenotech.com/>

operating close to their stall limit during maximum energy extraction. A comparison between full CFD and BEM of varying number of sections was performed by Lee et al [21], finding that whilst BEM methods produce reasonable results at a low computational cost, full scale FSI was still needed to capture complex flow physics. This includes out of plane effects, which become of increasing importance in blades with large prebend and large expected tip deflections. This is also significant in the context of FSI of occluded turbines, as the impact of vortex buffeting is one of the key areas of interest.

The choice of governing fluid equations to solve in the high fidelity solution is driven by the unsteady nature of the vortex shedding problem. Previous works have focussed on aerodynamic simulations solving both the Unsteady-Reynolds Averaged Navier-Stokes (URANS) equations [22], as well as Large Eddy Simulation (LES) equations [23]. LES methods have been found to produce more accurate results than URANS methods, particularly in unsteady vortex dominated flows such as those encountered in turbine wakes [12]. For FSI studies however, the difficulty encountered with extracting accurate boundary forces from LES models, as well as the increased computational cost means URANS remains the preferred method. A number of FSI studies have been performed examining the NREL phase VI reference turbine [21, 24], NREL 5MW turbine [8], MEXICO reference turbine [24], and DTU 10MW reference turbine [9].

The state-of-the-art work presented here investigates the FSI behaviour of a turbine blades using a high-fidelity, multi-physics framework. Both isolated turbines and those operating in the fully-occluded wake of another are considered. This is done using a fully-meshed modelling strategy with full flowfield calculations coupled to a structural solver through a unified data interpolation and mesh motion framework.

III. Problem Set-Up

Throughout this paper, a modified version of the 15MW reference turbine created as part of IEA Wind TCP Task 37 is used [25]. This blade is designed to be reflective of next-generation offshore turbines, with a total turbine radius (blade length) of 120m. The extremely large size of this blade makes it an ideal test case for FSI. Only the aerodynamic section of the blade is modelled (i.e. the circular root is omitted) and is meshed with prebend to enable accurate modelling of the aero-structural interaction. Finally, the trailing edge of the blade is also clam-shelled shut to create a sharp trailing edge. The aerofoil stack of the modelled blade is shown in Figure 2.

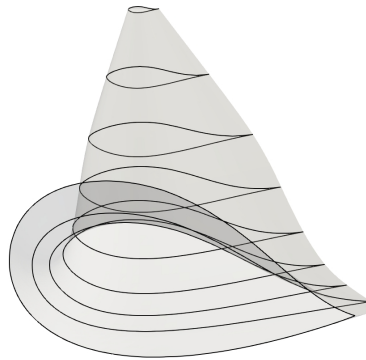


Fig. 2 Aerofoil stack

For this work, isolated turbines in freestream flow are considered. In regular operation, turbines normally operate in an atmospheric boundary layer (ABL) leading to asymmetric oncoming velocity across the disk, and with the coupling of tower effects. However, to ensure correct development of the aero-structural solver, uniform freestream velocity is considered initially; future work will look to introduce further effects including an ABL, tower, and hub. Due to a uniform oncoming flow, periodicity can be exploited. In the case of the 15MW, which is three-bladed, only a single fully-meshed blade in a 120° domain need to be modelled for the isolated turbine. This is shown schematically in Figure 3.

Two cases are considered: the first is a single, unyawed, isolated turbine subject to freestream flow; the second is an upstream turbine subject to freestream flow and a downstream turbine fully-occluded within the wake of the upstream one, with both turbines unyawed and 5D (1200m) apart from one another. For the fully-occluded case, two 120° domains are placed end-on. This models both turbines rotating in-phase at the same speed. Since, by 5D downstream, a turbine wake has fully-formed into a gross flow with a wake deficit, this is a fine assumption. To represent two turbines with

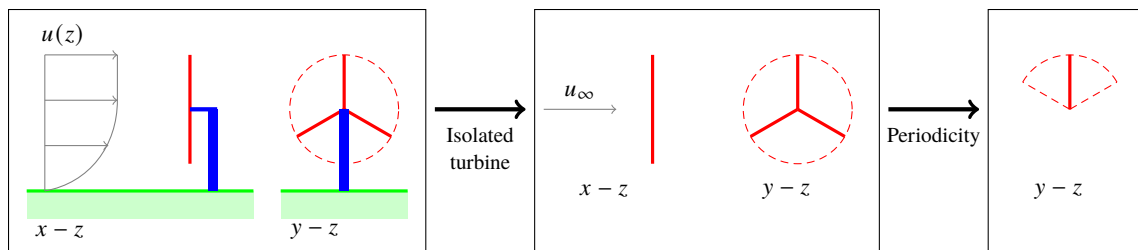


Fig. 3 Modelling strategy employed

out-of-phase and/or with different rotational speeds, a full 360° domain would be required.

The simulated flow condition is the worst-case scenario from an operational standpoint. The oncoming air is a uniform freestream at sea-level conditions with a velocity of 25m s^{-1} , which is the cut-out speed of the IEA 15MW. The turbine is run at a tip-speed of 95m s^{-1} , which is the maximum tip-speed of the IEA 15MW.

IV. Aero-Structural Solver

In this section, the CFD solver, structural solver and coupling approach are detailed. Details of GPU implementation are also given.

A. Flow Solver

The CFD solver zCFD[†] by Zenotech is used, which uses an unstructured mesh format. For viscous simulations, the RANS equations are solved using a cell-centred finite volume scheme, with 3rd order spatial accuracy. Turbulence is simulated through the use of Menter's SST turbulence model [26], with the addition of wall functions in the presence of large initial cell heights. Time marching is achieved through a five-stage Runge-Kutta scheme, with local timestepping and geometric multigrid to accelerate convergence. For inviscid simulations, the Euler equations are solved using the same finite volume and temporal integration schemes.

This solver takes advantage of parallelisation through METIS partitioning, and GPU acceleration through CUDA. Parallelisation across multiple cores is achieved through the use of MPI and OpenMP. The code is run on multiple P100 GPU cores split across multiple nodes on the University of Bristol's Blue Crystal Phase 4 cluster[‡].

This high level of parallelisation allows for easy simulation of large scale problems. An example of the application of this solver to wind energy applications is the RANS simulation of Horns Rev wind farm using actuator disks, shown in Figure 4. This simulation uses a 20 million cell unstructured mesh, with 80 turbine zones using uniform actuator disks reflective of Vestas V-80 turbines. The free stream velocity is set to 8m s^{-1} at hub height, with a wind direction of 280° . This example is intended to serve as a demonstration of the solver's capabilities and applicability to wind energy applications.

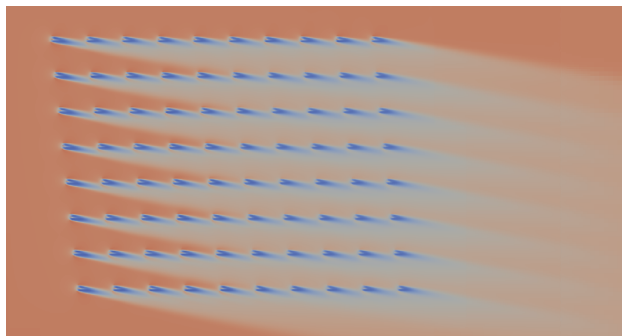


Fig. 4 Simulated hub-height velocity magnitude of Horns Rev

[†]<https://zenotech.com/zcfd-zenotech-computational-fluid-dynamics/>

[‡]<https://www.bristol.ac.uk/acrc/>

B. Meshing

The meshes used in this study are structured multiblock periodic meshes, generated using the software developed by Allen [27, 28]. The mesh uses a C-H topology wrapped around the blade, which can be seen in Figure 5. Improvements in mesh generation are achieved through orthogonal smoothing and transfinite interpolation [29]. Whilst studies have been conducted using unstructured meshes, such as that of Wang *et al.* [30], a structured mesh is preferred in this study due to the improved accuracy at the blade surface, ensuring accurate loadings are obtained to translate to the structural model.

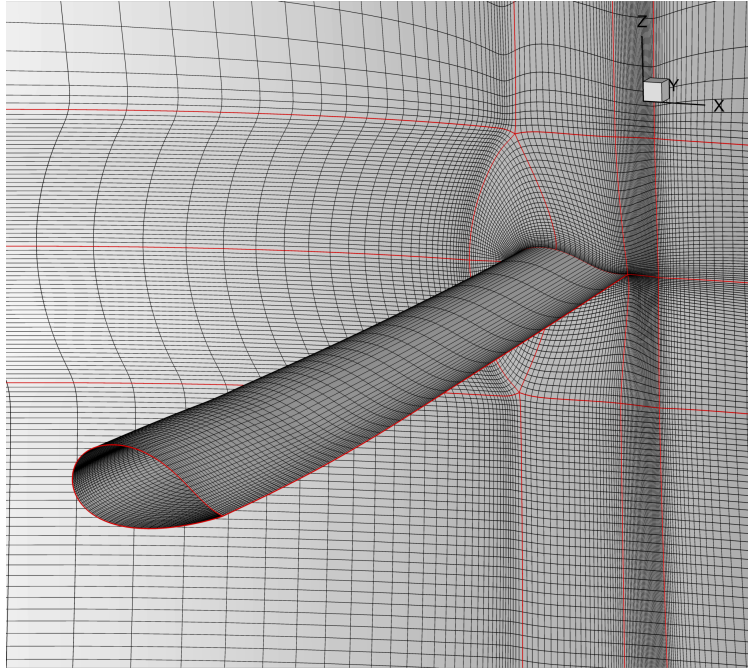


Fig. 5 Multiblock mesh topology at k=50 plane (0.49R)

C. Solver and Mesh Validation

The rotary mesh function of the solver and the mesh generation has been validated using the Caradonna-Tung rotor [31]. The Caradonna-Tung rotor is a 2-bladed rotor with each blade having an aspect ratio of 6, and a constant NACA0012 profile. Two test cases were simulated that had typical tip speeds of a wind turbine. Both have an 8° collective angle with tip Mach numbers of 0.225 and 0.439. A 5.5 million cell 180° periodic volume mesh is used, shown in Figure 6, with the surface mesh shown in Figure 7.

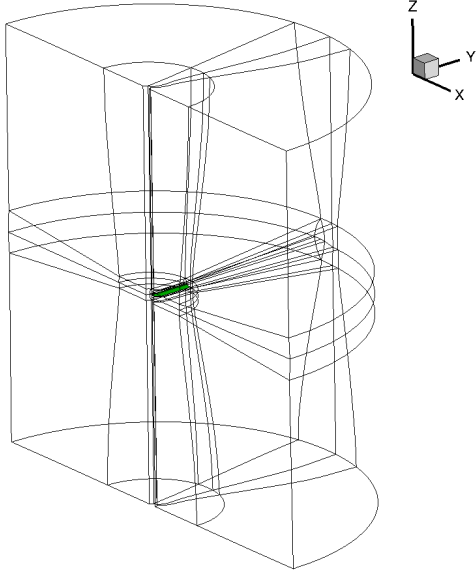


Fig. 6 Caradonna-Tung block structure

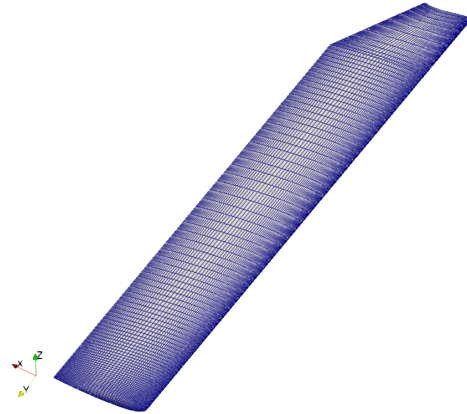


Fig. 7 Caradonna-Tung surface mesh

Viscous simulations using Menter’s SST turbulence model [26] with wall functions is used, with five-stage Runge-Kutta time-marching, and multigrid acceleration. The solver is run on the University of Bristol’s parallel HPC cluster- Blue Crystal Phase 4. A single node is exclusively used, utilising 2 NVIDIA P100 GPUs.

The resulting flowfield of the higher speed case is shown in Figure 8, with an iso-surface of eddy viscosity and blade surface pressures. Comparison of the experimental surface pressure distributions of the two cases is shown in shown in Figure 9, showing excellent agreement across the blade span for both test cases.

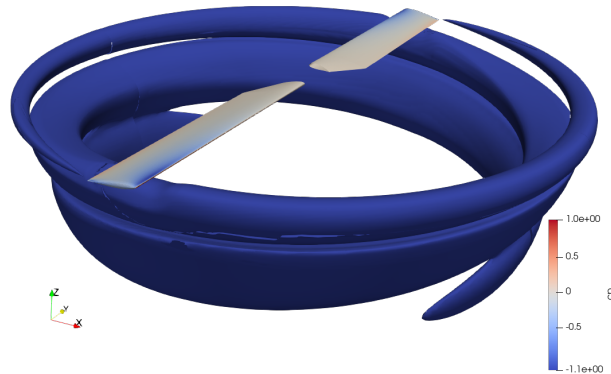


Fig. 8 Iso-surface for Eddy Viscosity for $M_{tip} = 0.439$ Caradonna-Tung test case

D. Structural Solver

The structural solver is from the University of Bristol’s Aeroelastic Turbine Optimisation Methods (ATOM) [32, 33] tool. ATOM is a full wind turbine optimisation framework that uses a blade element momentum (BEM) model to determine aerodynamic forces and a variety of structural solvers, including both linear and non-linear finite element with static and dynamic equations. For this work, the finite element modal solver in ATOM is employed. The structural model and modes of the IEA 15MW turbine are predefined and used directly in ATOM. A 43-node beam-stick model and the first six structural modes are used here. Figure 10 shows the structural model inside the blade surface, which

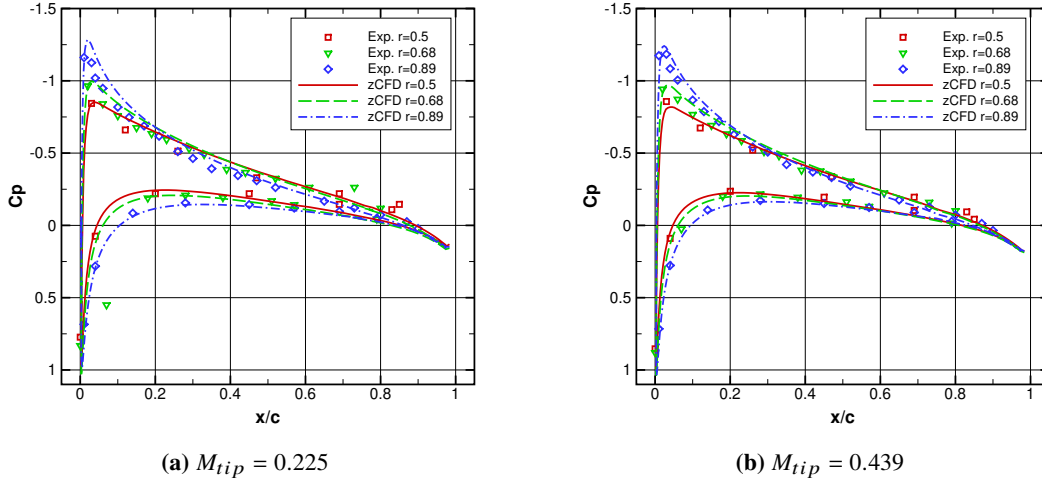


Fig. 9 Comparison of simulated surface pressure coefficients with experiment for Caradonna-Tung rotor at two different rotation speeds

shows the undeflected blade and the blade after a BEM-coupled structural solution with ATOM).

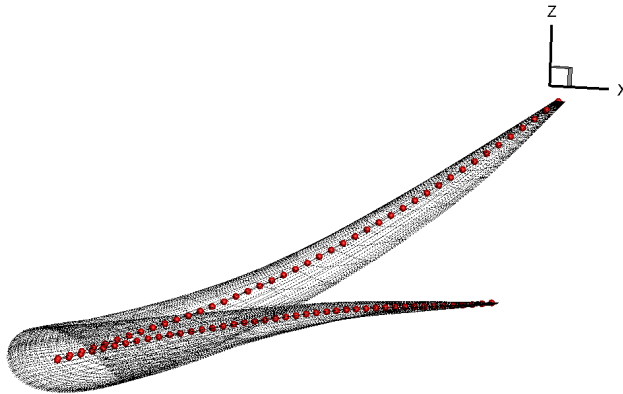


Fig. 10 Structural nodes of IEA 15MW model (undeflected and deformed after an ATOM (BEM) solve)

E. CFD-CSD Coupling Scheme

In order to solve FSI problems, two separate solutions need to be obtained- the aerodynamic solution, and the structural solution. These can either be solved using a single combined code- known as the Monolithic method, or through two separate specialised solvers, which are then coupled via methods such as Spring Analogy, Constant Volume Transforms (CVT), or Radial Basis Functions (RBF). In recent years the separated approach has become more popular, facilitated by advances in schemes used to couple the two results. Due to different requirements for CFD and CSD solvers the meshes used will be different (and likely, non-coincident), and will therefore require information to be transferred between surface nodes of each mesh. The structural mesh requires surface forces to be transferred from the aerodynamic surface to the structural surface, and the aerodynamic mesh requires the transfer of structural mesh displacements to the aerodynamic surface.

The manner in which this coupling is achieved can be broken down into three categories depending on how information is transferred at each time step. A schematic demonstrating this information transfer is shown in Figure 11, where f represents a force data transfer, and Δx represents a displacement transfer. Loose coupling [8, 21] performs a one way information transfer at the same time step. Staggered coupling [9] iterates the two solutions at slightly different time steps. Strong coupling [24, 34] performs multiple information transfers per time step, ensuring the result is fully converged at each point in time. Strong coupling comes at the highest computational cost, but provides the most accurate

results, particularly for unsteady effects such as flutter and buffeting.

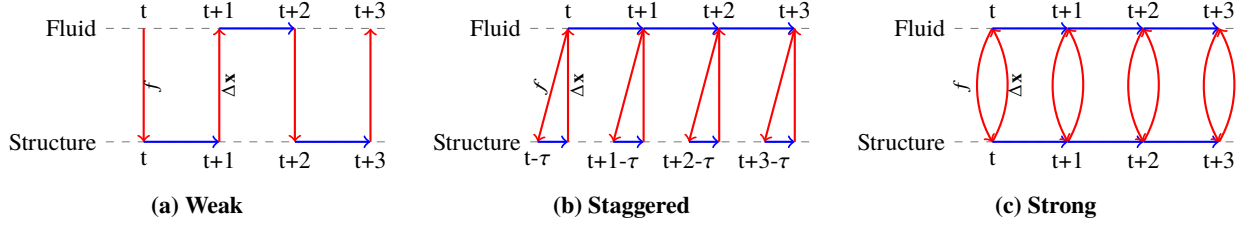


Fig. 11 Schematic of different coupling schemes

Whilst a 2016 study by Heinz et al found that loose coupling is generally sufficient for generating accurate FSI results for high fidelity turbine simulations [35], this was proven on single turbines under steady inflow conditions. Due to the highly unsteady nature of this problem and the complex flow physics to be encountered however, strong coupling is used throughout this work. Initially just a single steady state loop is solved until the solution is fully converged. Solving to this state in pseudo time allows for unsteady solutions to be obtained through marching the same scheme in real time.

1. Radial Basis Function Interpolation

Coupling between the aerodynamic surface and structural model is achieved through the use of a multivariate volume interpolation using Radial Basis Functions (RBFs), as outlined by Rendall and Allen [36]. RBFs have the benefit of being both mesh and connectivity independent; provided a list of surface nodes for both the aerodynamic and structural surfaces, the information can easily be transferred. The theory of RBFs is presented comprehensively by Buhmann [37] and Wendland [38], while the formulation pertaining to the data interpolation is presented here. A real function, $f(\mathbf{x})$, can be approximated by fitting an interpolation function, $s(\mathbf{x})$, through N known data sites, where the i -th data site in three-dimensional space is $\mathbf{x}_i = [x_i, y_i, z_i]^T$. The interpolation at a point in space, $\mathbf{x} = [x, y, z]^T$, is then given by:

$$f(\mathbf{x}) \approx s(\mathbf{x}) = \sum_{i=1}^N \alpha_i \phi(\|\mathbf{x} - \mathbf{x}_i\|) + p(\mathbf{x}) \quad (1)$$

where α_i is an RBF coefficient, ϕ is the RBF function adopted (such as a Wendland functions [38]), and $p(\mathbf{x})$ is an optional polynomial. The polynomial can be used in mesh motion to recover translation and rotation, though is often omitted to avoid motion of the farfield. However, at least a linear polynomial must be included for the data transfer between aerodynamic and structural nodes to ensure conservation of total force and moment. A linear polynomial in the x -direction (equivalent y and z expressions are also formed) is of the form:

$$p^x(\mathbf{x}) = \gamma_0^x + \gamma_x^x x + \gamma_y^x y + \gamma_z^x z \quad (2)$$

The RBF coefficients α_i can be found through requiring exact recovery of the original function at the known data sites. In the presence of the polynomial, the system is completed by the ‘side condition’:

$$\sum_{i=1}^N \alpha_i q(\mathbf{x}) = 0 \quad \forall q(\mathbf{x}) \mid \deg q(\mathbf{x}) \leq \deg p(\mathbf{x}) \quad (3)$$

The compact generic matrix formulation of the generic system is now presented. Setting-up an interpolation between a set of control sites, $\{\mathbf{x}_{c1}, \dots, \mathbf{x}_{cN}\}$, requiring exact recovery at the sites and using the side condition, the system is written as:

$$\mathbf{X} = \mathbf{\Phi}_{cc} \boldsymbol{\alpha}^x \quad (4)$$

$$\mathbf{Y} = \mathbf{\Phi}_{cc} \boldsymbol{\alpha}^y \quad (5)$$

$$\mathbf{Z} = \mathbf{\Phi}_{cc} \boldsymbol{\alpha}^z \quad (6)$$

where:

$$\mathbf{X}_c = \begin{bmatrix} 0 \\ 0 \\ 0 \\ 0 \\ x_{c_1} \\ \vdots \\ x_{c_N} \end{bmatrix}, \mathbf{\Phi}_{cc} = \begin{bmatrix} 0 & 0 & 0 & 0 & 1 & \dots & 1 \\ 0 & 0 & 0 & 0 & x_{c_1} & \dots & x_{c_N} \\ 0 & 0 & 0 & 0 & y_{c_1} & \dots & y_{c_N} \\ 0 & 0 & 0 & 0 & z_{c_1} & \dots & z_{c_N} \\ 1 & x_{c_1} & y_{c_1} & z_{c_1} & \phi_{c_1,c_1} & \dots & \phi_{c_1,c_N} \\ \vdots & \vdots & \vdots & \vdots & \vdots & \ddots & \vdots \\ 1 & x_{c_N} & y_{c_N} & z_{c_N} & \phi_{c_N,c_1} & \dots & \phi_{c_N,c_N} \end{bmatrix}, \boldsymbol{\alpha}^x = \begin{bmatrix} \gamma_0^x \\ \gamma_x^x \\ \gamma_y^x \\ \gamma_z^x \\ \alpha_1^x \\ \vdots \\ \alpha_N^x \end{bmatrix} \quad (7)$$

(with analogous definitions for y and z) and:

$$\phi_{c_i,c_j} = \phi(\|\mathbf{x}_{c_i} - \mathbf{x}_{c_j}\|) \quad (8)$$

Hence, $\mathbf{\Phi}_{cc}$ is the matrix of RBFs evaluated between all of the control sites and is size $N + 4 \times N + 4$. The system is solved to find the RBF coefficients:

$$\boldsymbol{\alpha}^x = \mathbf{\Phi}_{cc}^{-1} \mathbf{X}_c \quad (9)$$

$$\boldsymbol{\alpha}^y = \mathbf{\Phi}_{cc}^{-1} \mathbf{Y}_c \quad (10)$$

$$\boldsymbol{\alpha}^z = \mathbf{\Phi}_{cc}^{-1} \mathbf{Z}_c \quad (11)$$

Once the interpolation is constructed, it can be evaluated at M number of evaluation sites, $\{\mathbf{x}_{e_1}, \dots, \mathbf{x}_{e_M}\}$ from equation 1, which in compact form is given by (with analogous definitions for y and z variables):

$$\mathbf{X}_e = \mathbf{\Psi}_{ec} \boldsymbol{\alpha}^x = \mathbf{\Psi}_{ec} \mathbf{\Phi}_{cc}^{-1} \mathbf{X} = \mathbf{H}_{ec} \mathbf{X}_c \quad (12)$$

where the coupling matrix $\mathbf{\Psi}$ is the matrix of RBFs (plus the polynomial terms if applicable) between the variable and evaluation sites:

$$\mathbf{\Psi} = \begin{bmatrix} 1 & x_{e_1} & y_{e_1} & z_{e_1} & \phi_{e_1,c_1} & \dots & \phi_{e_1,c_N} \\ \vdots & \vdots & \vdots & \vdots & \vdots & \ddots & \vdots \\ 1 & x_{e_M} & y_{e_M} & z_{e_M} & \phi_{e_M,c_1} & \dots & \phi_{e_M,c_N} \end{bmatrix}, \quad (13)$$

and \mathbf{H}_{ec} is termed the interpolation matrix. However, it should be noted that for memory efficiency reasons in the mesh motion, this matrix is never fully constructed. Rather, the interpolation is determined at each evaluation point individually, as explained in the ‘*operation-intensive*’ approach in Kedward *et al.* [39].

There are many forms for the RBF itself (e.g. Gaussian, thin plate spine, Euclid’s hat), but the functions of Wendland [38] provide a definable smoothness level and a definable radius of influence, as well as showing numerical properties suitable for these types of problems [36]. The C^2 function is used throughout, which varies by a distance r from a point of origin, given by:

$$\phi(r) = (1 - r)_+^4 (4r + 1) \quad (14)$$

where $(1 - r)_+$ is the ‘*cut-off*’ function which is $(1 - r)$ if $r \leq 1$, or 0 otherwise. The Euclidean distance argument of the RBF is therefore a scaled distance, which is scaled by the support radius, R . The support radius therefore controls the distance of influence of the interpolation and ensures compact support. Careful choice of the support radius is required to balance a smooth interpolation with a numerically stable system.

2. Data Interpolation

A two-way complementary data interpolation is formed to interpolate displacements from the structure to the aerodynamic surface, and the subsequent forces from the surface back to the structure. Structural nodal displacements, $[\Delta \mathbf{x}_s^T, \Delta \mathbf{y}_s^T, \Delta \mathbf{z}_s^T]^T$ are interpolated to aerodynamic surface nodal displacements by:

$$\Delta \mathbf{x}_a = \mathbf{H}_{as} \Delta \mathbf{x}_s \quad (15)$$

$$\Delta \mathbf{y}_a = \mathbf{H}_{as} \Delta \mathbf{y}_s \quad (16)$$

$$\Delta \mathbf{z}_a = \mathbf{H}_{as} \Delta \mathbf{z}_s \quad (17)$$

where the interpolation matrix \mathbf{H}_{as} is formed using the structural nodes as the control sites and the aerodynamic surface nodes as the evaluation sites.

The aerodynamic surface forces, $[\mathbf{f}_s^T, \mathbf{g}_s^T, \mathbf{h}_s^T]^T$, are interpolated to the structural nodes by:

$$\mathbf{f}_s = \mathbf{H}_{sa}^T \mathbf{f}_a \quad (18)$$

$$\mathbf{g}_s = \mathbf{H}_{sa}^T \mathbf{g}_a \quad (19)$$

$$\mathbf{h}_s = \mathbf{H}_{sa}^T \mathbf{h}_a \quad (20)$$

where the interpolation matrix \mathbf{H}_{sa} is formed using the aerodynamic surface nodes as the control sites and the structural nodes as the evaluation sites. For both interpolations, a linear polynomial is used to ensure conservation.

3. Mesh Motion

Once structural displacements are interpolated to the aerodynamic surface, the volume mesh must subsequently deform. For mesh deformation to occur, the farfield must remain fixed. For this, a compactly supported function is required with a support radius that does not extend to the farfield (if a non-compact function is used then farfield motion can be fixed by using the farfield nodes as control sites with a zero deformation specified), as well as omitting the polynomial. Deformation of the aerodynamic mesh points, $[\Delta \mathbf{x}_m^T, \Delta \mathbf{y}_m^T, \Delta \mathbf{z}_m^T]^T$ is given by:

$$\Delta \mathbf{x}_m = \mathbf{H}_{ma} \Delta \mathbf{x}_a \quad (21)$$

$$\Delta \mathbf{y}_m = \mathbf{H}_{ma} \Delta \mathbf{y}_a \quad (22)$$

$$\Delta \mathbf{z}_m = \mathbf{H}_{ma} \Delta \mathbf{z}_a \quad (23)$$

where the interpolation matrix \mathbf{H}_{ma} uses the aerodynamic surface points as control sites and the volume mesh as interpolation points. In the case of volume mesh displacement, the use of \mathbf{H}_{ma} is limited by memory due to its $N_m \times N_a$ in size where N_m is the number of volume mesh nodes, and N_a are the number of aerodynamic surface nodes. For the smaller 5 million cell turbine mesh this would correlate to an approximate $5,000,000 \times 20,000$ array, occupying 400GB of memory if floats are used. Instead, \mathbf{H}_{ma} is constructed row by row at each interpolation phase.

Constructing the interpolation matrix requires solving a $n_a \times n_a$ (where n_a is the number of aerodynamic surface points), which for large meshes becomes computationally difficult. To reduce the size of the system, work by Rendall and Allen [40] used a greedy point selection to reduce the number of surface points used. However, later work by Kedward *et al.* [39] superseded this by introducing the multiscale method. The multiscale RBF method is used here for mesh motion.

This unified coupling scheme allows the translation of forces from the aerodynamic surface onto the structural nodes, and then the subsequent structural deformations to the aerodynamic surface, and ultimately to the aerodynamic volume mesh. This procedure has been demonstrated to be effective in producing accurate high-fidelity aero-structural results [41].

F. Coupled Solver

The flow solver fits within an overall zCFD environment. The solver itself is partitioned into a front-end and back-end, with Python scripting handling the front-end. The ability to compute on both and GPUs is fully exploited here. Here, data interpolation and the structural solver are coupled into the zCFD environment front-end. Once data initialisation has occurred on the CPU, flow updates are performed on the GPU for rapid computation times. Data can be passed to and from the devices. For this work, aerodynamic surface forces are transferred to the CPU where the interpolations, structural solution and mesh motion are computed. The deformed mesh is then transferred back to the GPU for the ongoing flow updates. Figure 12 shows a schematic of the overall process, including key data flow between the devices. It should also be noted that during set-up, if a GPU is not available, the code can be run entirely on the CPU.

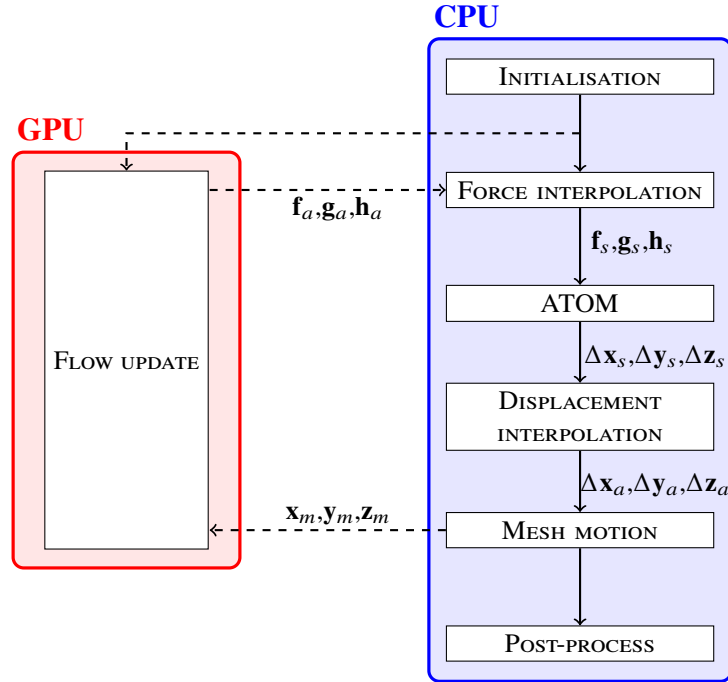


Fig. 12 Code structure and device workflow

V. Aerodynamic Simulations

Before progressing to fully-coupled simulations, aerodynamic simulations are presented of both the isolated turbine, and the two-turbine fully-occluded case. As shown in Figure 3, periodicity is employed for the cases meaning that the fully-occluded case is a simulation of two turbines rotating at the same speed in-phase with each other. The domain (and multi-block) structure is shown in Figure 13. Since the longitudinal separation between the turbines is 5-D, the wake of the upstream turbine is fully-developed into a gross wake deficit region, so any out-of-phase or minor difference in rotation speed would have a negligible effect.

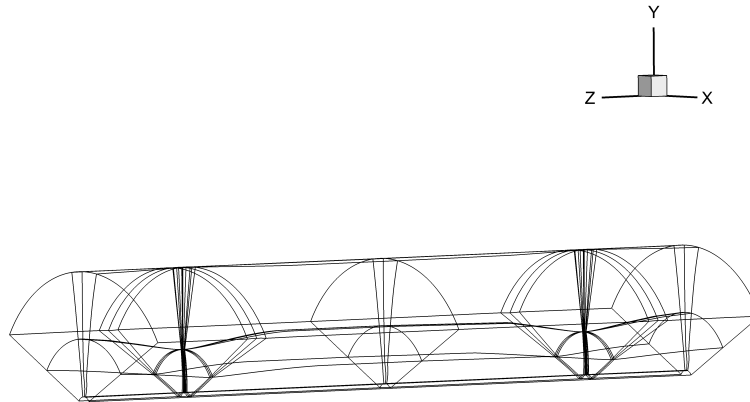


Fig. 13 Structure of occluded case

For the single turbine, a 5 million cell mesh is used, with refinement in the near wake. For the two turbine case, a 10 million cell mesh is used. The two turbines are spaced 5-D apart in the streamwise direction (no lateral offset) with a balance of refinement in the near wake of both turbines with good capture of the upstream turbine's far wake (i.e. between the turbines). The single turbine case was run to convergence on two P100 GPUs and took 4.2 hours, while the two turbine case was run on four GPUs for 13.5 hours. This solution was conservatively run to a much higher number of

iterations (40,000) to guarantee full wake propagation from the upstream to downstream turbine. Upon inspection of the convergence history and development of the flow solution it was found a converged solution was obtained in fewer than 10,000 cycles.

The near wake structure of the single turbine is shown in Figure 14, showing successful capture of the wake. The iso-surface, which is vorticity, clearly dissipates quickly and forms a gross wake deficit structure that is typical of wind turbines.

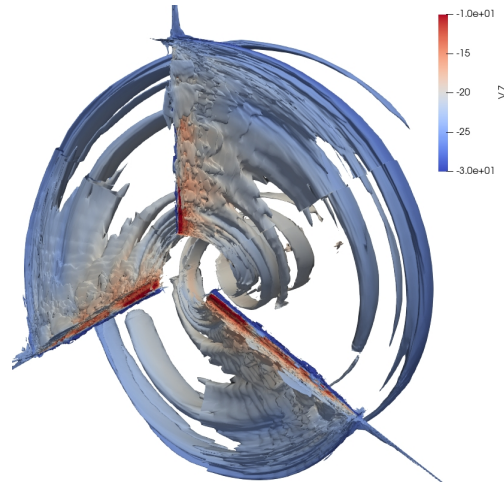


Fig. 14 Near-wake structure of isolated turbine

The surface pressure coefficient distributions of the two turbine case are shown in Figure 15, which shows both the upstream and downstream turbine. Three radial stations are shown (25%, 50% and 75%). It is first worth noting the extremely high suction peaks around the blades. However, these are inviscid simulations at low speed, so reductions in pressure peaks would be expected for viscous flows, or high speed flows causing shocks. These pressure peaks are a correct representation for these aerofoil sections in inviscid flow. Furthermore, it is clear the occluded (downstream) turbine has a lower overall loading across the blade. Considering Figure 16 also (which gives streamwise velocity), the upstream wake is occluding the downstream turbine, as expected.

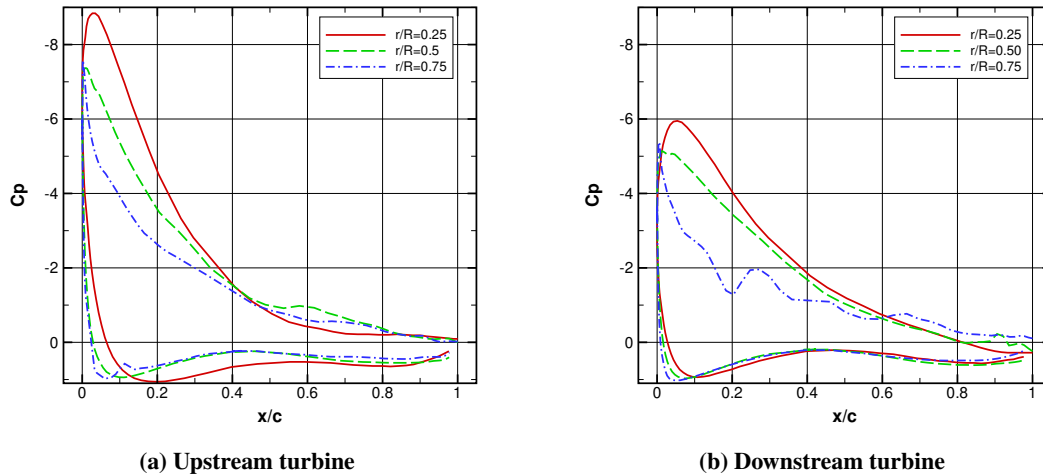


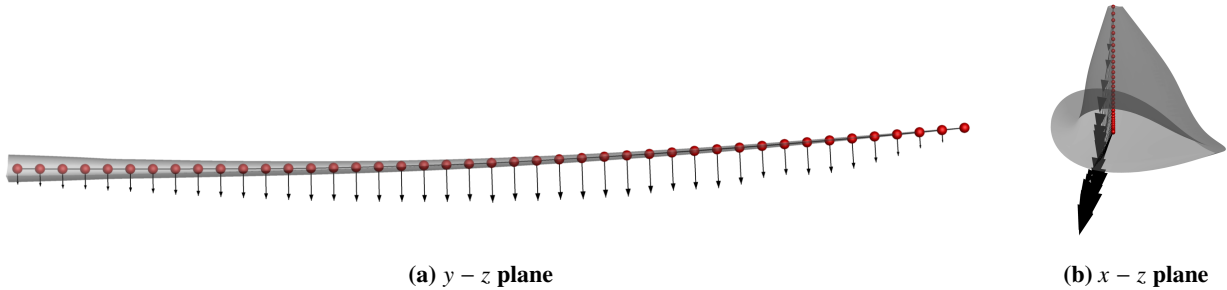
Fig. 15 Surface pressure coefficients of upstream and downstream turbines



Fig. 16 Occluded case streamwise velocity contours

VI. Aero-Structural Simulations

As the aerodynamic simulations show the expected behaviour, aero-structural simulations were subsequently run for the occluded case. To do this, the converged aerodynamic solution was used to initiate the flow. Subsequent coupling cycles were performed which involved a structural solution for each turbine followed by further flow solver iterations to obtain a converged solution per coupled cycle until full convergence was achieved. Interpolated forces on the structural model are shown in Figure 17.



(a) $y - z$ plane

(b) $x - z$ plane

Fig. 17 Loaded structural model

The final converged solution of the downstream turbine blade is shown in Figure 18. The final deflection at the tip of the aeroelastic blade is 2.23m. The full solution took 15.5 hours to run on four P100 GPUs, which was made up of 13.5 hours for the initial flow solution and 2 hours for the coupling cycles.

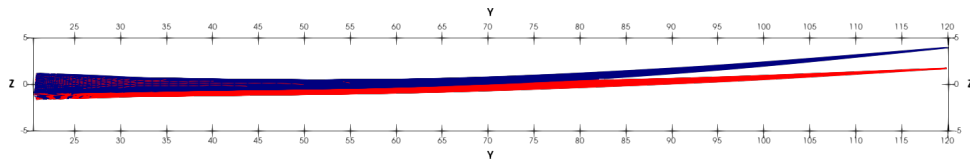


Fig. 18 Occluded turbine blade static (blue) and aeroelastic (red) solution

VII. Conclusions and Future work

A high-fidelity aerodynamic-structural coupled simulation framework has been presented and applied to flexible wind turbines. The GPU-enabled flow solver framework, zCFD, has been used to couple the solver with a structural model via a radial basis function interpolation. The flow solver has the ability to run on CPUs and GPUs making the framework powerful and flexible, with large efficiency gains possible.

The primary case considered is where a wind turbine is fully-occluded by the wake of an upstream turbine. A 10 million cell aerodynamic mesh is used to ensure good capture of the wake occlusion, and its effect on the downstream turbine. The turbine blade used was a modified version of the IEA 15MW turbine, and was run at the IE 15MW maximum tip speed and maximum flow speed. The solution was run on four NVIDIA P100 GPUs, with a full Euler flow solution on the undeformed mesh performed initially followed by coupling iterations. While only inviscid flow was considered initially to test the framework, expected results were obtained with the 120m radius turbine having a 2.2m tip deflection.

Future work will move towards performing viscous simulations and develop the framework further to be able to perform dynamic simulations to assess fatigue. In the long-term this work will look to include the atmospheric boundary layer and demonstrate a variety of test cases to show the flexibility of the developed framework.

VIII. Acknowledgements

This work was undertaken with funding from the UK Engineering and Physical Sciences Research Council Doctoral Training Programme EP/R513179/1. The HPC resources of Bristol ACRC[§] were used for numerical simulations, notably Blue Crystal Phase 4 for highly parallel GPU simulations. The authors would like to thank David Standingford, James Sharpe, and the other staff at Zenotech for their continued support and collaboration throughout the project. Thanks also to Sam Scott and Terence Macquart for providing and supporting ATOM.

References

- [1] United Nations, Department of Economic and Social Affairs, Population Division, “World Population Prospects 2019: Ten Key Findings,” 2019.
- [2] U.S. Energy Information Administration, “International Energy Outlook 2019,” 2019.
- [3] Burton, T., Jenkins, N., Sharpe, D., and Bossanyi, E., *Wind Energy Handbook*, 2nd ed., Wiley, John Wiley & Sons LTD, The Atrium, Southern Gate, Chichester, West Sussex, PO19 8SQ, United Kingdom, 2011.
- [4] Jonkman, J., Butterfield, S., Musial, W., and Scott, G., “Definition of a 5-MW Reference Wind Turbine for Offshore System Development,” Tech. rep., National Renewable Energy Laboratory, 2009.
- [5] Bak, C., Zahle, F., Bische, R., Kim, T., Yde, A., Henriksen, L. C., Natarajan, A., and Hansen, M., “Description of the DTU 10MW Reference Wind Turbine,” Tech. rep., DTU Wind Energy, 2013.
- [6] “GE Haliade X Specifications,” URL <https://www.ge.com/renewableenergy/wind-energy/offshore-wind/haliade-x-offshore-turbine>, accessed: 8-12-2020.
- [7] “Siemens 12MW turbine specifications,” URL <https://www.siemensgamesa.com/en-int/products-and-services/offshore/wind-turbine-sg-14-222-dd>, accessed: 8-12-2020.
- [8] Dose, B., Rahimi, H., Herráez, I., Stoevesandt, B., and Peinke, J., “Fluid-structure coupled computations of the NREL 5MW wind turbine by means of CFD,” *Renewable Energy*, Vol. 129, 2018, pp. 591–605.
- [9] Sayed, M., Lutz, T., Krämer, E., Shayegan, S., and Wüchner, R., “Aeroelastic analysis of 10MW wind turbine using CFD-CSD explicit FSI-coupling approach,” *Journal of Fluids and Structures*, Vol. 87, 2019, pp. 354–377.
- [10] O’Brien, J., Young, T., O’Mahoney, D., and Griffin, P., “Horizontal axis wind turbine research: A review of commercial CFD, FE codes and experimental practices,” *Progress in Aerospace Sciences*, Vol. 92, 2017, pp. 1–24.
- [11] Bai, C.-J., and Wang, W.-C., “Review of computational and experimental approaches to analysis of aerodynamic performance in horizontal-axis wind turbines,” *Renewable and Sustainable Energy Reviews*, Vol. 63, 2016, pp. 506–519.
- [12] Thé, J., and Yu, H., “A critical review on the simulations of wind turbine aerodynamics focusing on hybrid RANS-LES methods,” *Energy*, Vol. 138, 2017, pp. 257–289.
- [13] Troldborg, N., “Actuator Line Modeling of Wind Turbine Wakes,” Ph.D. thesis, Department of Mechanical Engineering, Technical University of Denmark, 2008.
- [14] Sørensen, J., and Shen, W. Z., “Numerical Modeling of Wind Turbine Wakes,” *Journal of Fluids Engineering*, Vol. 124, 2002, pp. 393–399.
- [15] Shen, W. Z., Sørensen, J. N., and Zhang, J., “Actuator surface model for wind turbine flow computations,” *Proceedings of European Wind Energy Conference*, 2007.
- [16] Fischer, G. R., Kipouros, T., and Savill, A. M., “Multi-objective optimisation of horizontal axis wind turbine structure and energy production using aerofoil and blade properties as design variables,” *Renewable Energy*, Vol. 62, 2014, pp. 506–515.

[§]<https://www.bristol.ac.uk/acrc/>

- [17] Monte, A. D., Betta, S. D., Castelli, M. R., and Benini, E., "Proposal for a coupled aerodynamic-structural wind turbine blade optimization," *Composite Structures*, Vol. 159, 2017, pp. 144–156.
- [18] Yang, H., Chen, J., Pang, X., and Chen, G., "A new aero-structural optimization method for wind turbine blades used in low wind speed areas," *Composite Structures*, Vol. 207, 2019, pp. 446–459.
- [19] Boujleben, A., Ibrahimbegovic, A., and Lefrançois, E., "An efficient computational model for fluid-structure interaction in application to a large overall motion of wind turbine with flexible blades," *Applied Mathematical Modelling*, Vol. 77, 2020, pp. 392–407.
- [20] Sessarego, M., Feng, J., Ramos-García, N., and Horcas, S. G., "Design optimization of a curved wind turbine blade using neural networks and an aero-elastic vortex method under turbulent inflow," *Renewable Energy*, Vol. 146, 2020, pp. 1524–1535.
- [21] Lee, K., Huque, Z., Kommalapati, R., and Han, S.-E., "Fluid-structure interaction analysis of NREL phase VI wind turbine: Aerodynamic force evaluation and structural analysis using FSI analysis," *Renewable Energy*, Vol. 113, 2017, pp. 512–531.
- [22] Lienard, C., Boisard, R., and Daudin, C., "Aerodynamic behavior of a floating offshore wind turbine," *AIAA SciTech Forum*, Washington, DC, 2019. AIAA Paper 2019-1575.
- [23] Sedaghatizadeh, N., Arjomandi, M., Kelso, R., and Cazzolato, B., "Modelling of wind turbine wake using large eddy simulation," *Renewable Energy*, Vol. 115, 2018, pp. 1166–1176.
- [24] Carrion, M., Steijl, R., Woodgate, M., Barakos, G., and Munduate, X., "Aeroelastic analysis of wind turbines using a tightly coupled CFD–CSD method," *Journal of Fluids and Structures*, Vol. 50, 2014, pp. 392–415.
- [25] Gaertner, E., Rinker, J., Sethuraman, L., Zahle, F., Anderson, B., Barter, G., Abbas, N., Meng, F., Bortolotti, P., Skrzypinski, W., Scott, G., Feil, R., Bredmose, H., Dykes, K., Shields, M., and Viselli, C. A. A., "Definition of the IEA 15-Megawatt Offshore Reference Wind Turbine," Tech. rep., National Renewable Energy Laboratory, 2020.
- [26] Menter, F., "Two-Equation Eddy-Viscosity Turbulence Models for Engineering Applications," *AIAA Journal*, Vol. 32, 1994, pp. 1598–1605.
- [27] Allen, C., "Multigrid convergence of inviscid fixed- and rotary-wing flows," *International Journal for Numerical Methods in Fluids*, Vol. 39, 2002, pp. 121–140.
- [28] Allen, C., "Parallel simulation of unsteady hovering rotor wakes," *International Journal for Numerical Methods in Engineering*, Vol. 68, 2006, pp. 632–649.
- [29] Allen, C., "Towards automatic structured multiblock mesh generation using improved transfinite interpolation," *International Journal for Numerical Methods in Engineering*, Vol. 74, 2008, pp. 697–733.
- [30] Wang, L., Quant, R., and Kolios, A., "Fluid structure interaction modelling of horizontal-axis wind turbine blades based on CFD and FEA," *Journal of Wind Engineering and Industrial Aerodynamics*, Vol. 158, 2016, pp. 11–25.
- [31] Caradonna, F. X., and Tung, C., "Experimental and Analytical Studies of a Model Helicopter Rotor in Hover," Tech. rep., NASA Technical Memorandum 81232, 1981.
- [32] Macquart, T., Maes, V., Langston, D., Pirrera, A., and Weaver, P., "A New Optimisation Framework for Investigating Wind Turbine Blade Designs," *12th World Congress on Structural and Multidisciplinary Optimization*, Braunschweig, Germany, 2017.
- [33] Scott, S., Macquart, T., Robriquez, C., Greaves, P., McKeever, P., Weaver, P., and Pirrera, A., "Preliminary validation of ATOM: an aero-servo-elastic design tool for next generation wind turbines," *WindEurope Conference and Exhibition 2019*, Bilbao, Spain, 2019. Published in *Journal of Physics: Conference Series*, Volume 1222.
- [34] Santo, G., Peeters, M., Paepegem, W. V., and Degroote, J., "Dynamic load and stress analysis of a large horizontal axis wind turbine using a full scale fluid-structure interaction simulation," *Renewable Energy*, Vol. 140, 2019, pp. 212–226.
- [35] Heinz, J. C., Sørensen, N. N., and Zahle, F., "Fluid-structure interaction computations for geometrically resolved rotor simulations using CFD," *Wind Energy*, Vol. 19, 2016, pp. 2205–2221.
- [36] Rendall, T., and Allen, C., "Unified fluid-structure interpolation and mesh motion using radial basis functions," *International Journal for Numerical Methods in Engineering*, Vol. 74, 2008, pp. 1219–1559.
- [37] Buhmann, M. D., *Radial Basis Functions*, 1st ed., Cambridge University Press, Cambridge, United Kingdom, 2003.

- [38] Wendland, H., *Scattered Data Approximation*, 1st ed., Cambridge University Press, Cambridge, United Kingdom, 2005.
- [39] Kedward, L., Allen, C. B., and Rendall, T. C., “Efficient and exact mesh deformation using multiscale RFC interpolation,” *Journal of Computational Physics*, Vol. 345, 2017, pp. 732–751.
- [40] Rendall, T., and Allen, C., “Efficient mesh motion using radial basis functions with data reduction algorithms,” *Journal of Computational Physics*, Vol. 228, 2009, pp. 6231–6249.
- [41] Poole, D., Allen, C., and Rendall, T., “Efficient Aero-Structural Wing Optimization Using Compact Aerofoil Decomposition,” *AIAA SciTech Forum*, Washington, DC, 2019. AIAA Paper 2019-1701.